Nonradiative charge transfer in collisions of protons with rubidium atoms*

Yan Ling-Ling(闫玲玲)[a], Qu Yi-Zhi(屈一至)[a)†], Liu Chun-Hua(刘春华)[b)c)], Zhang Yu(张 宇)[b)], Wang Jian-Guo(王建国)[b)], and Buenker Robert J[d)]

[a)] *College of Material Sciences and Optoelectronic Technology, Graduate University of the Chinese Academy of Sciences, Beijing* 100049, *China*

[b)] *The Key Laboratory of Computational Physics, Institute of Applied Physics and Computational Mathematics, Beijing* 100088, *China*

[c)] *Institute of Modern Physics, Chinese Academy of Sciences, Lanzhou* 730000, *China*

[d)] *Fachbereich C-Mathematik und Naturwissenschaften, Bergische Universität Wuppertal, D*-42097 *Wuppertal, Germany*

(Received 8 October 2011; revised manuscript received 15 November 2011)

The nonradiative charge-transfer cross sections for protons colliding with Rb(5s) atoms are calculated by using the quantum-mechanical molecularorbital close-coupling method in an energy range of 10^{-3} keV–10 keV. The total and state-selective charge-transfer cross sections are in good agreement with the experimental data in the relatively low energy region. The importance of rotational coupling for chargetransfer process is stressed. Compared with the radiative charge-transfer process, nonradiative charge transfer is a dominant mechanism at energies above 15 eV. The resonance structures of state-selective charge-transfer cross sections arising from the competition among channels are analysed in detail. The radiative and nonradiative charge-transfer rate coefficients from low to high temperature are presented.

Keywords: charge transfer, proton–rubidium collisions, cross section

PACS: 34.10.+x, 34.70.+e **DOI:** 10.1088/1674-1056/21/6/063401

1. Introduction

The charge-transfer reaction is an important atomic collision process, and it has been studied extensively in the past several decades.[1−4] The charge-transfer cross sections for proton–rubidium collisions have been measured in many experiments since the early 1970s. Using a slow proton source and a rubidium container as the target, Girnius *et al.*,[4] and Ebel and Salzborn[5] have measured the total charge-transfer cross sections for energies above 0.2 keV. Utilizing the proton beam obtained from the electron-bombardment ion source and the rubidium target cell, the total and state-selective charge-transfer cross sections have been measured by Nagata,[6] and Nagata and Kuribara[7] in the energy ranges of 0.4 keV–5.0 keV and 0.06 keV–5.0 keV, respectively. These earlier measurements of total cross sections are generally in good agreement with each other.

The proton–rubidium collision system has also been stimulated in some theoretical studies in the 1980s. The pioneering work of Kubach and Sidis[8] was based on a simplified one-electron projected-valence-bond approximation method. The total charge-transfer cross sections in an energy range of 0.2 keV–6.0 keV were obtained from seven-state close-coupling calculations. Their calculated cross sections for energies above 0.6 keV are in agreement with the experimental measurements.[4−6] Later, an impact-parameter perturbed-stationary-state theory with associated molecular electron translation factors (ETF) was employed by Kimura and Olson[9] to calculate the total and state-selective charge-transfer cross sections at energies from 0.2 keV to 6.0 keV. At relatively high energies ($E > 0.6$ keV), the Kimura and Olson's cross section displays a more rapidly decreasing tendency toward higher energies than Kubach and Sidis's.[8] For energies below 0.6 keV, the total cross sections calculated by Kubach and Sidis[8] and by Kimura and Olson[9] both show some discrepancies relative to the experimental data. A recent theoretical study with adopting the Faddeev three-body equation approach

*Project supported by the National Natural Science Foundation of China (Grant Nos. 10979007, 11025417, 11179041, and 11004014) and the NSAF (Grant No. 10876043).

†Corresponding author. E-mail: yzqu@gucas.ac.cn

© 2012 Chinese Physical Society and IOP Publishing Ltd

by Avakov *et al.*[10] reported on the total and state-selective charge-transfer cross sections in the energy range of 0.1 keV–400 keV, but the total cross section exceeds previous experimental and theoretical studies[4−6,8−10] over the entire incident energy region. It should be noted that in the previous theoretical studies[8−10] the collision process was treated as a quasi-one-electron system and the excitation of the innershell electrons of the RbH^+ system was not described thereby. In order to understand the discrepancies among the different theories and experiments, further theoretical and experimental investigations are required.

In the present work, charge-transfer processes $H^+ + Rb(5s) \rightarrow H(n = 2) + Rb^+$ due to collision of ground-state rubidium atoms with protons are re-examined by using a quantum-mechanical molecular-orbital close coupling (QMOCC) method. In the current QMOCC calculations we utilize the adiabatic potentials, radial and rotational coupling matrix elements obtained by employing the *ab initio* multireference single- and double-excitation configuration interaction (MRD-CI) method. For proton–rubidium collisions, the outer nine valence electrons of rubidium are involved. Total and state-selective cross sections are calculated and compared with the available theoretical and experimental results. The rest of the present paper is organized as follows. In Section 2 described are the molecular potential and coupling data utilized in the QMOCC calculations, while in Section 3 the scattering calculation approach is discussed. In Section 4 presented are the results of the scattering calculation including comparisons of total and state-selective cross sections and rate coefficients with those of other calculations and experiments. A brief summary is given in Section 5. Atomic units are used throughout the paper unless otherwise noted.

2. Electronic structure calculation

In the present study, *ab initio* multireference configuration interaction calculations are carried out for adiabatic potential energies of five $^2\Sigma^+$ states in A_1 (C_{2v}) symmetry and two $^2\Pi$ states in B_1 symmetry of the RbH^+ system by employing the MRD-CI package.[11,12] For the hydrogen atom the cc-pVQZ correlation-consistent, polarization valence, a quadruple zeta basis set[13] is used, and 2s, 2p diffuse functions are added to describe the Rydberg states. For the rubidium atom, an effective core potential (ECP)[14] is employed to describe the twenty-eight core electrons. The remaining nine valence electrons are considered explicitly in the *ab initio* self-consistent-field and CI calculations. The ECP-adapted (5s, 5p) Gaussian basis set without contraction is utilized to describe the 4s, 4p, and 5s subshells. In addition, a diffuse basis (1s, 1p, 4d, 2f) is employed for describing its Rydberg states. A threshold of 2×10^{-11} Hartree is applied to the selection of the configuration wave functions for RbH^+. The errors in the asymptotic energies of the relevant electronic states are in the hundreds of cm^{-1} range as given in Table 1. The obtained electronic wave functions are then employed to calculate radial and rotational couplings by using finite differentiation and analytical approaches, respectively.[15]

Table 1. Asymptotic separated-atom energies for the states of RbH^+.

Molecular states	Asymptotic atomic states	Energy/cm^{-1}		
		NIST	MRDCI	Error
1-$^2\Sigma^+$	Rb^++ H(1s)	–75988	–76872	884
2-$^2\Sigma^+$	Rb(5s)+ H^+	0	0	0
3-$^2\Sigma^+$	Rb^++ H(2p)	6271	5493	777
1-$^2\Pi$	Rb^++ H(2p)	6271	5496	775
4-$^2\Sigma^+$	Rb^++ H(2s)	6271	5501	770
5-$^2\Sigma^+$	Rb(5p)+ H^+	12737	12197	540
2-$^2\Pi$	Rb(5p)+ H^+	12737	12197	540

The adiabatic potential energy curves each as a function of internuclear distance R are shown in Fig. 1. The 1-$^2\Sigma^+$ state is not included since the potential curve has no appreciable interaction with the other states. The 2-$^2\Sigma^+$ state represents the initial channel for our considered processes. Each potential curve for the 2-$^2\Sigma^+$, 3 $^2\Sigma^+$, 1-$^2\Pi$, and 2-$^2\Pi$ states has one well in the small-R region which is caused by the excitation

of the inner-4p-shell electrons of the Rb atom. However, these wells did not appear in other theoretical studies,[8,9] in which the RbH^+ molecule was treated as an effective one-electron system and the inner-4p-shell electrons were not excited. The 3-$^2\Sigma^+$, 4-$^2\Sigma^+$, and 1-$^2\Pi$ states act as the charge-transfer channels. There exist a broad avoided crossing between the 2-$^2\Sigma^+$ and 3-$^2\Sigma^+$ states and a strongly avoided crossing between the 3-$^2\Sigma^+$ and 4-$^2\Sigma^+$ states, which accord with the Kubach and Sidis's[8] and Kimura and Olson's results.[9] These crossings are important for the charge-transfer dynamics in the considered collision energy region. In addition, the 1-$^2\Pi$ state potential crosses that of the 3-$^2\Sigma^+$ state at large R, and approaches the 2-$^2\Sigma^+$ state potential at small R, which is also a significant charge-transfer channel through the rotational-coupling mechanism.

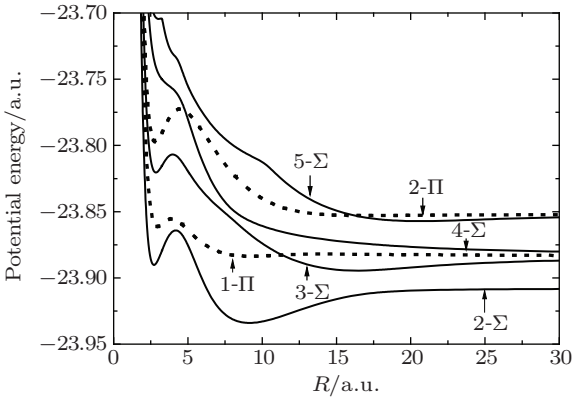


Fig. 1. Adiabatic potential curves for RbH^+ each as a function of internuclear distance, where solid lines are for the $^2\Sigma^+$ channels and dotted lines for the $^2\Pi$ channels. The 2-$^2\Sigma^+$, 3-$^2\Sigma^+$, 4-$^2\Sigma^+$, 5-$^2\Sigma^+$, 1-$^2\Pi$, and 2-$^2\Pi$ states correspond to the Rb(5s)+H^+, Rb^++H(2pσ), Rb^++H(2s), Rb(5pσ)+H^+, Rb^++H(2pπ), and Rb(5pπ)+H^+ states in the asymptotic regions, respectively.

Figure 2 displays the non-adiabatic radial coupling matrix elements, which are calculated by finite difference approximation as

$$A_{ij} = \left\langle \psi_i \left| \frac{\partial}{\partial R} \right| \psi_j \right\rangle = \lim_{\Delta R \to 0} \frac{1}{\Delta R} \langle \psi_i(R + \Delta R) \rangle$$

with a step size of 0.0002 a.u. The positions of the peaks in the radial couplings are consistent with the avoided crossings of the adiabatic potentials. The 2-$^2\Sigma^+$–3-$^2\Sigma^+$ radial coupling has three peaks at R = 2.5, 4.9, and 16.5 a.u, respectively. The calculated R = 16.5 a.u. broad peak is in agreement with Kimura and Olson's result.[9] The 3-$^2\Sigma^+$–4-$^2\Sigma^+$ radial coupling exhibits two sharp peaks at R = 4.1 and 7.8 a.u., respectively. The 2-$^2\Sigma^+$–3-$^2\Sigma^+$ and 3-$^2\Sigma^+$–4-$^2\Sigma^+$ couplings will govern the charge-exchange process because of their large values. Although the radial coupling for the 4-$^2\Sigma^+$–5-$^2\Sigma^+$ states is strong, there is a relatively large energy gap between the 5-$^2\Sigma^+$ and (initial) 2-$^2\Sigma^+$ channels. The 5-$^2\Sigma^+$ channel will play an important role in collision-excitation cross sections at high energies ($E > 10$ keV), but in the present work we do not consider this excitation process.

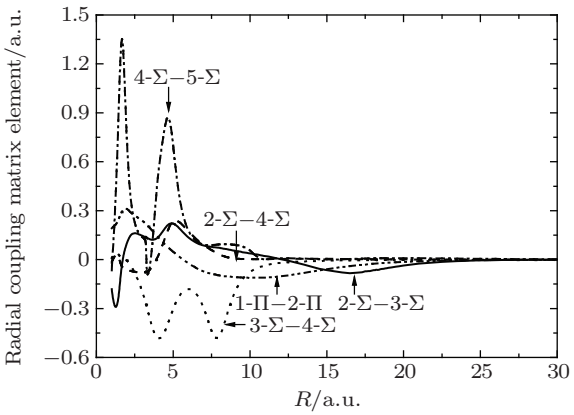


Fig. 2. Radial coupling matrix elements for RbH^+.

In Fig. 3 some important adiabatic rotational coupling matrix elements $A^{\theta}_{ij} = \langle \psi_i | \, \mathrm{i} L_y \, | \psi_j \rangle$ are displayed. Rotational couplings (for 2-$^2\Sigma^+$–1-$^2\Pi$, 2-$^2\Sigma^+$–2-$^2\Pi$, 3-$^2\Sigma^+$–2-$^2\Pi$ states) approach zero at large R since they correspond to different configurations. The couplings between the same atomic configurations, the 3-$^2\Sigma^+$–1-$^2\Pi$ and the 4-$^2\Sigma^+$–1-$^2\Pi$ have the same asymptotical value of 0.75 a.u. The 2-$^2\Sigma^+$–1-$^2\Pi$ rotational couplings show two broad maxima at R = 2.6 a.u. and 14.2 a.u., respectively, which implies that the 1-$^2\Pi$ state may be a major channel in the charge-transfer process. Kimura and Olson[9] have mentioned the strong rotational

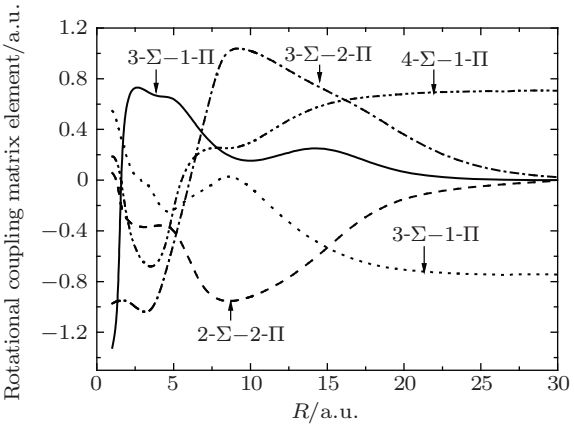


Fig. 3. Rotational coupling matrix elements for RbH^+.

coupling between the initial 2-$^2\Sigma^+$ and the final 1-$^2\Pi$ state for small-impact-parameter collisions, and this will be confirmed in our subsequent cross section calculations.

3. Theoretical approach

The QMOCC method used to describe charge transfer in ion–atom collisions has been formulated,[16,17] and here we only outline it briefly. It involves solving a coupled set of second-order differential equations by using the log-derivative method.[18] In the adiabatic representation, transitions between channels are driven by elements (radial A^R and rotational A^θ) of the vector potential $A(\boldsymbol{R})$, where $\boldsymbol{R}$ is the internuclear distance vector. Since the adiabatic description contains first-order derivatives, it is numerically convenient to make a unitary transformation[16,19] to a diabatic representation as shown below:

$$U(R) = W(R)[V(R) - P(R)]W^{-1}(R), \qquad (1)$$

where $U(R)$ is the diabatic potential matrix, $V(R)$ is the diagonal adiabatic potential, $W(R)$ is a unitary transformation matrix, and $P(R)$ is the rotational matrix of the vector potential $A(\boldsymbol{R})$.

With the diabatic potentials and couplings, the coupled set of second-order differential equations is solved to obtain the K matrix from the scattering amplitude after a partial-wave decomposition.[16] The charge-transfer cross section from initial channel i to final channel j is then given by

$$\sigma_{(i\to j)} = \frac{\pi}{k_i^2}\sum_J (2J+1)|S_J|^2_{i,j}, \qquad (2)$$

where k_i is the initial momentum, J is the total angular momentum, and the S matrix is

$$S_J = [I + \mathrm{i}K_J]^{-1}[I - \mathrm{i}K_J], \qquad (3)$$

and I is the identity matrix. In the present work, the electron translation factors (ETFs) (see Ref. [20]), which are often used to modify the molecular eigenfunctions to remove asymptotic couplings between atomic states, are not included. The influence of ETFs is expected to be important for $E > 1$ keV–5 keV (e.g., Ref. [21]), which is close to the maximal calculated energy in the present work.

4. Results and discussion

4.1. Total charge-transfer cross sections

Using the QMOCC method, total charge-transfer cross sections for proton–rubidium collisions are calculated in an energy range of 0.03 keV–10 keV.

The calculations are carried out for the two cases, with and without rotational couplings, and the results are displayed in Fig. 4(a). Firstly, we check the convergence. Without rotational couplings, the QMOCC calculations are carried out for three $^2\Sigma^+$ channels and four $^2\Sigma^+$ channels. The differences in total cross section are within 8%. With rotational couplings, the calculations are carried out for the three $^2\Sigma^+$ channels and one $^2\Pi$ channel, and for the four $^2\Sigma^+$ and two $^2\Pi$ channels. The differences are within 9% for $E < 3$ keV. This demonstrates that our calculations

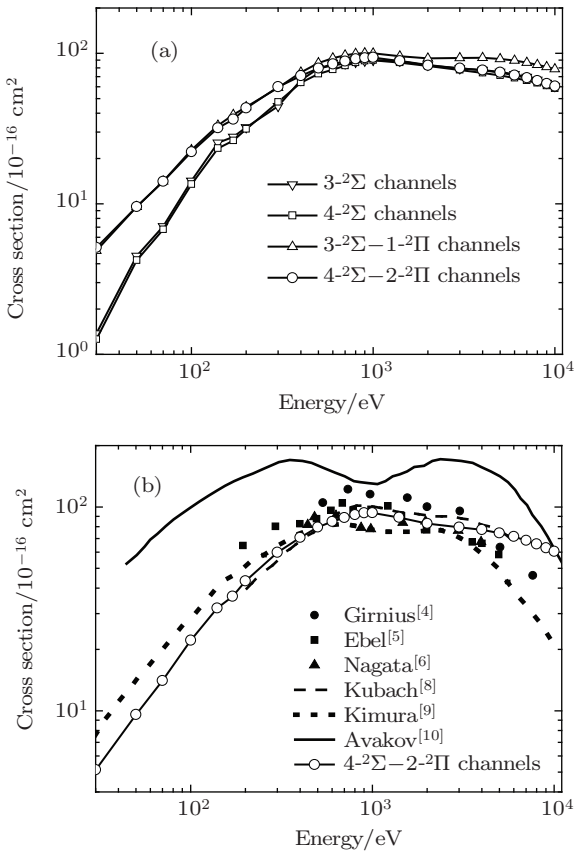


Fig. 4. Total nonradiative charge-transfer cross sections versus energy. Panel (a) is for the present calculations with different channels, and panel (b) for the comparisons between the present results and other calculations and measurements. The theoretical results are the present calculations (solid line with open symbols) and those that are cited from the papers by Kubach *et al.*[8] (dashed line), Kimura *et al.*[9] (dotted line), and Avakov *et al.*[10] (solid line). Experimental results are cited from the papers by Girnius *et al.*[4] (solid circles), Ebel *et al.*[5] (solid squares), and Nagata *et al.*[6] (solid up-triangles).

are sufficiently converged. The rotational coupling is important in the energy region considered, especially when $E < 0.4$ keV. For example, inclusion of rotational coupling increases the cross section up to 200% at 0.03 keV. Similar results have been obtained for the proton–sodium and proton–potassium collision processes.[22,23] In addition, for $E > 1$ keV, there appears to be a significant difference in cross sections between including one-$^2\Pi$ state and two-$^2\Pi$ states (i.e., through rotational coupling). Including more rotational coupling interactions show better agreement with the pure radial coupling calculations.

Comparisons between the present QMOCC results and other available calculations and measurements are shown in Fig. 4(b). The results given by Kubach and Sidis,[8] and Kimura and Olson[9] and the present calculations are in general agreement with the experimental measurements. The present total cross sections lie between the calculations by Kubach and Sidis,[8] and Kimura and Olson.[9] For $E > 4.0$ keV, the experiments and calculations of Kimura and Olson[9] display a more rapidly decreasing cross section toward higher energies, whereas the present and the Kubach and Sidis's[8] cross sections decrease gradually. This difference is due probably to the fact that we have not included ETFs, which may be important in the relatively high-energy region.

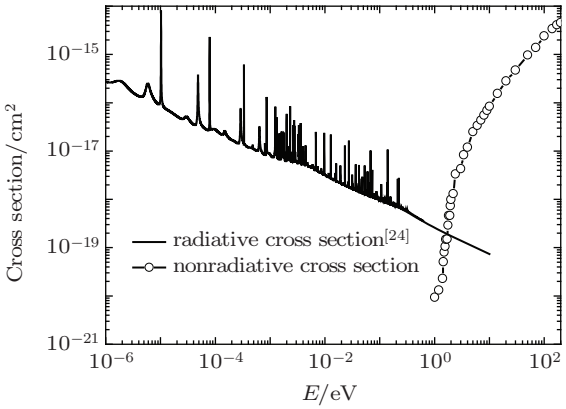


Fig. 5. Nonradiative- and radiative-decay charge transfer cross sections, where the present nonradiative cross section is denoted by solid line with open circles, the radiative-decay cross section[24] by solid line.

Figure 5 shows the total charge-transfer cross sections for proton–rubidium collisions in the low-energy range of 10^{-3} keV–0.2 keV. The radiative-decay cross sections obtained by using the optical potential method and semi-classical methods,[24] respectively, are compared. For $E < 1.5$ eV, the radiative process is a dominant charge-transfer mechanism, while as the energy increases, the radiative cross section decreases and the nonradiative charge-transfer cross section rapidly increases. For $E > 1.5$ eV, nonradiative charge transfer becomes a dominant mechanism.

4.2. State-selective charge transfer cross sections

Figure 6 displays the state-selective cross sections for electron capture to H(2s) and H(2p) states in comparison with other available calculations and measurements. The QMOCC cross sections are calculated including four $^2\Sigma^+$ and two $^2\Pi$ channels. Capture to H(2p) dominates in the entire energy region. This is because the initial channel 2-$^2\Sigma^+$∼Rb(5s)+H$^+$ and charge-transfer channels 3-$^2\Sigma^+$∼Rb$^+$+H(2pσ) and 1-$^2\Pi$∼Rb$^+$+H(2pπ) are very close in energy to each other and relatively strong interactions exist among these channels.

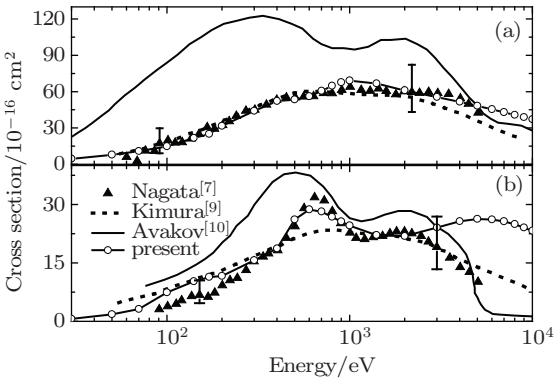


Fig. 6. State-selective charge-transfer cross sections. Panel (a) is for the electron capture to state H(2p), and panel (b) for the capture to state H(2s). The theoretical results are the present calculation (solid line with open circles), and those that are cited from the papers by Kimura *et al.*[9] (dotted line) and Avakov *et al.*[10] (solid line). The experimental results are cited from the paper by Nagata *et al.*[7] (solid up-triangles).

The present state-selective cross sections are in good agreement with the measurements of Nagata and Kuribara[7] within experimental error. At relatively high energies ($E > 3$ keV), the present cross sections for electron capture to H(2s) are larger than the measurements. This is again because ETFs are not included in the present work. In the low-energy region, the theoretical calculations by Avakov *et al.*[10] are higher than the present and the Kimura and Olson's[9] results. The present state-selective cross sections are in good agreement with Kimura and Olson's[9] data. At energies from 0.4 keV to 2.0 keV, the present calculations for capture to H(2s) and measurements[7] show a similar resonance structure, probably produced by

the channel competition, while Kimura and Olson's results[9] do not exhibit such a structure. The reason is that the RbH^+ collision process calculated by Kimura and Olson[9] is considered as a quasi-one-electron system, and the couplings between initial and final channels in the small R region may therefore be inaccurate.

To investigate the competition among channels in the charge-transfer process, the state-selective cross sections for captures to 3-$^2\Sigma^+\sim$ Rb^++H(2pσ), 4 $^2\Sigma^+\sim$ Rb^++H(2s), and 1-$^2\Pi$ $\sim$$Rb^+$+H(2p$\pi$) states are given in Fig. 7. The calculations include four $^2\Sigma^+$ and two $^2\Pi$ channels.

In the low-energy range ($E < 0.08$ keV), the state-selective cross sections for electron capture to the 1-$^2\Pi$ state dominate. When the energy increases, the cross sections for captures to the 3-$^2\Sigma^+$, 4-$^2\Sigma^+$, and 1-$^2\Pi$ channels compete with each other. The cross section to the 3-$^2\Sigma^+$ channel rapidly exceeds that to the 1-$^2\Pi$ channel. The 3-$^2\Sigma^+$ state becomes a dominant charge-transfer final channel, which is caused by the broad radial coupling between the 2-$^2\Sigma^+$–3-$^2\Sigma^+$ states in large R region. At energies from 0.4 keV to 2.0 keV, 1-$^2\Pi$ state is temporarily far away from the 2-$^2\Sigma^+$state, so the cross section to the 1-$^2\Pi$ channel decreases. The cross sections for captures to the 3-$^2\Sigma^+$ and 4-$^2\Sigma^+$ channels both display a maximum. This is because at $R \sim 5$ a.u. there exist strong radial couplings between the initial channel (2-$^2\Sigma^+$) and the charge-transfer channels (3-$^2\Sigma^+$ and 4-$^2\Sigma^+$). For energies above 2 keV, because the 1-$^2\Pi$ state is close to the 2-$^2\Sigma^+$ state, the cross section for capture to the 3-$^2\Sigma^+$ channel starts to decrease, whereas the cross section for capture to the 1-$^2\Pi$ channel shows a broad maximum.

The peak of the cross sections for capture to H(2s) at an energy of 0.64 keV displayed in Fig. 6(b) corresponds to the maximum of the state-selective cross section for capture to the 4-$^2\Sigma^+$ channel. The weak resonance structures of the cross sections for capture to the H(2p) found in experiment[7] arise from the charge-transfer competition between the 3-$^2\Sigma^+$ and 1-$^2\Pi$ channels. In the relatively high-energy region ($E > 2$ keV), it is not possible to obtain the broad peak[7] of the cross sections for capture to the 4-$^2\Sigma^+$ channel, which is perhaps a consequence of carrying out the calculations at high energy without using ETFs.

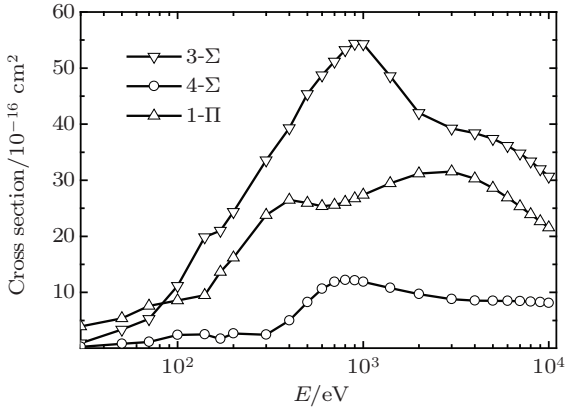


Fig. 7. State-selective charge-transfer cross sections for captures to the 3-$^2\Sigma^+$, 4-$^2\Sigma^+$, and 1-$^2\Pi$ states.

4.3. Rate coefficients

The rate coefficients are obtained by integrating the corresponding radiative and nonradiative cross sections over a Maxwellian velocity distribution.

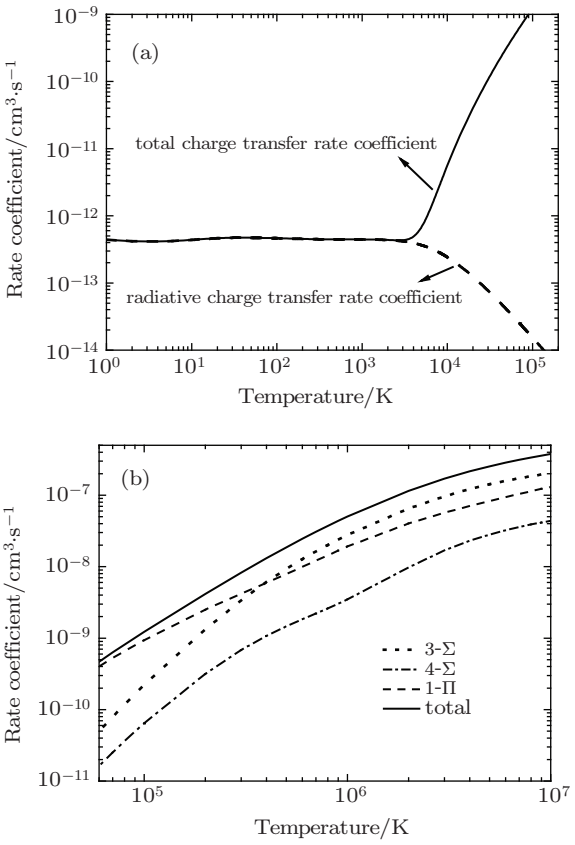


Fig. 8. Charge-transfer rate coefficients each as a function of temperature. Panel (a) is for the radiative and total charge-transfer rate coefficients, panel (b) for the total and state-selective charge-transfer rate coefficients.

Comparison between the radiative and the total (including both radiative and nonradiative) charge-transfer rate coefficients as a function of temperature T from 1 K to 2×10^4 K is given in Fig. 8(a).

For $T < 4 \times 10^3$ K, the rate coefficient approaches a constant value of approximately 4.45×10^{-13} cm^3·s^{-1}, which is due mainly to the radiative process. As the temperature increases, the radiative rate coefficient decreases, while the total charge-transfer rate coefficient rapidly increases. This is because the nonradiative charge-transfer process dominates at energies above 1.5 eV. In Fig. 8(b), the state-selective charge-transfer rate coefficients are displayed. The rate coefficients of the 3-$^2\Sigma^+$ and 4-$^2\Sigma^+$ states are much larger than those of 1-$^2\Pi$ state. As the temperature increases, the rate coefficient of the 3-$^2\Sigma^+$ state ascends sharply. Its value exceeds that of the 4-$^2\Sigma^+$ state at $T \sim 3.8 \times 10^5$ K, which better reflects the state-selective charge-transfer process. For convenience in future applications, some numerical data and fittings to these rate coefficients are presented in Tables 2 and 3. The fitting errors are less than 3%.

Table 2. Radiative and total charge-transfer rate coefficients. Fitting parameters a_i (cm^3·s^{-1}), b_i, and c_i (K) for the relations $\alpha(T) = \sum_i a_i\,(T/10000)^{b_i} \exp(-T/c_i)$ are also given (numbers in square brackets denote powers of 10).

Temperature T/K	Rate coefficient α/cm^3·s^{-1}	
	Radiative charge transfer	Total charge transfer
1.0	4.40[−13]	4.40[−13]
2.0	4.19[−13]	4.19[−13]
4.0	4.15[−13]	4.15[−13]
8.0	4.30[−13]	4.30[−13]
10	4.38[−13]	4.38[−13]
20	4.64[−13]	4.64[−13]
40	4.73[−13]	4.73[−13]
80	4.67[−13]	4.67[−13]
100	4.64[−13]	4.64[−13]
200	4.53[−13]	4.53[−13]
400	4.46[−13]	4.46[−13]
800	4.45[−13]	4.45[−13]
1000	4.45[−13]	4.45[−13]
2000	4.37[−13]	4.37[−13]
4000	4.91[−13]	3.94[−13]
8000	2.72[−12]	2.85[−13]
10000	5.61[−12]	2.42[−13]
20000	4.02[−11]	1.24[−13]
a_1	–3.63[−11]	6.54[−12]
b_1	1.98	2.52
c_1	7.62[3]	1.36[3]
a_2	1.13[−11]	1.12[−10]
b_2	1.28	1.25
c_2	–3.26[4]	3.34[1]
a_3	6.00[−13]	4.87[−13]
b_3	4.07[−2]	1.85[−2]
c_3	7.96[2]	1.40[4]

Table 3. State-selective charge-transfer rate coefficients. Fitting parameters a_i (cm^3·s^{-1}), b_i, and c_i (K) for the relations $\alpha(T) = \sum_i a_i\,(T/10000)^{b_i} \exp(-T/c_i)$ are also given (numbers in square brackets denote powers of 10).

Temperature $T/10^4$ K	Rate coefficient α/cm^3·s^{-1}			
	3-$^2\Sigma^+$	4-$^2\Sigma^+$	1-$^2\Pi$	Total
20	1.33[−9]	3.16[−10]	2.51[−9]	4.15[−9]
30	3.37[−9]	6.84[−10]	4.17[−9]	8.23[−9]
40	6.13[−9]	1.08[−9]	5.94[−9]	1.32[−8]
50	9.33[−9]	1.47[−9]	7.87[−9]	1.87[−8]

Table 3. (*Continued*).

Temperature $T/10^4$ K	Rate coefficient α/cm^3·s^{-1}			
	3-$^2\Sigma^+$	4-$^2\Sigma^+$	1-$^2\Pi$	Total
60	1.28[−8]	1.84[−9]	9.95[−9]	2.46[−8]
70	1.64 [−8]	2.21[−9]	1.22[−8]	3.08[−8]
80	2.02[−8]	2.60[−9]	1.45[−8]	3.72[−8]
90	2.39[−8]	3.02[−9]	1.68[−8]	4.38[−8]
100	2.78[−8]	3.47[−9]	1.92[−8]	5.04[−8]
200	6.49[−8]	9.76[−9]	4.03[−8]	5.04[−8]
300	9.66[−8]	1.69[−8]	5.69[−8]	1.15 [−7]
400	1.22[−7]	2.31[−8]	7.07[−8]	1.71[−7]
500	1.42[−7]	2.82[−8]	8.30[−8]	2.16[−7]
600	1.59[−7]	3.24[−8]	9.42[−8]	2.54[−7]
700	1.73[−7]	3.59[−8]	1.04[−7]	2.86[−7]
800	1.85[−7]	3.89[−8]	1.14[−7]	3.13[−7]
900	1.95[−7]	4.16[−8]	1.23[−7]	3.37[−7]
1000	2.04[−7]	4.39[−8]	1.31[−7]	3.59[−7]
a_1	–2.22[−1]	1.43[−7]	–2.60[-6]	1.53[−9]
b_1	2.12	4.93[−1]	6.46[−1]	2.58[1]
c_1	2.54[5]	–1.17[7]	1.14[6]	3.15[4]
a_2	7.12[−3]	7.51[−5]	6.97[−3]	–7.20[−5]
b_2	1.64	1.13	2.12	1.41
c_2	3.41[7]	9.20[5]	1.28[7]	1.86[6]
a_3	–6.17[−2]	–3.29[−5]	1.26[−6]	1.74[−3]
b_3	1.92	9.88[−1]	5.69[−1]	1.69
c_3	1.60[8]	1.15[6]	3.86[6]	2.64[7]

5. Conclusion

In the present paper, nonradiative charge-transfer processes for protons colliding with Rb(5s) atoms are investigated utilizing the quantum-mechanical molecular-orbital close-coupling method. Total and state-selective charge-transfer cross sections are presented. The present total and state-selective cross sections are in good agreement with the available experimental data in the low energy region, however there exist significant differences in the high energy region ($E > 2$ keV), and ETF may be one reason, which will be considered in future. The importance of rotational coupling for charge-transfer processes is stressed. In the energy region $E > 1.5$ eV, the nonradiative charge-transfer process dominates over the charge-transfer mechanism. The competition among channels explains the generation of resonance structures in the state-selective cross sections. Finally, the radiative and nonradiative charge-transfer rate coefficients are presented.

References

[1] Wang F and Wang M M 2011 *Chin. Phys.* B **20** 113402
[2] Lu Y X, Lu X Q, Song X and Zhang B L 2011 *Chin. Phys.* B **20** 033402
[3] Wu Y, Liu L and Wang J G 2008 *Acta Phys. Sin.* **57** 947 (in Chinese)
[4] Girnius R J, Anderson L W and Staab E 1977 *Nucl. Instrum. Methods* **143** 505
[5] Ebel F and Salzborn E 1987 *J. Phys.* B **20** 4531
[6] Nagata T 1980 *J. Phys. Soc. Jpn.* **48** 2068
[7] Nagata T and Kuribara M 1986 *J. Phys. Soc. Jpn.* **55** 500
[8] Kubach C and Sidis V 1981 *Phys. Rev.* A **23** 110
[9] Kimura M and Olson R E 1982 *Phys. Rev.* A **26** 3113
[10] Avakov G V, Blokhintsev L D, Kadyrov A S and Mukhamedzhanov A M 1992 *J. Phys.* B **25** 213
[11] Buenker R J and Phillips R A 1985 *J. Mol. Struct. THEOCHEM* **123** 291
[12] Krebs S and Buenker R J 1995 *J. Chem. Phys.* **103** 5613
[13] Dunning T H Jr 1989 *J. Chem. Phys.* **90** 1007
[14] LaJohn L A, Christiansen P A, Ross R B, Atashroo T and Ermler W C 1987 *J. Chem. Phys.* **87** 2812
[15] Hirsch G, Bruna P J, Buenker R J and Peyerimhoff S D 1980 *Chem. Phys.* **45** 335
[16] Zygelman B and Dalgarno A 1986 *Phys. Rev.* A **33** 3853
[17] Kimura M and Lane N F 1990 *Adv. At. Mol. Phys.* **26** 79
[18] Johnson B R 1973 *J. Comput. Phys.* **13** 445
[19] Heil T G, Butler S E and Dalgarno A 1981 *Phys. Rev.* A **23** 1100
[20] Errea L F, Méndez L and Riera A 1982 *J. Phys.* B **15** 101
[21] Errea L F, Harel C, Jouin H, Mendez L, Pons B and Rioera A 1994 *J. Phys.* B **27** 3603
[22] Liu C H, Qu Y Z, Liu L, Wang J Q, Li Y, Liebermann H P, Funke P and Buenker R J 2008 *Phys. Rev.* A **78** 024703
[23] Liu C H, Qu Y Z, Wang J Q, Li Y and Buenker R J 2010 *Phys. Rev.* A **81** 012707
[24] Zhou Y, Qu Y Z, Liu C H and Liu X J 2011 *Chin. Phys. Lett.* **28** 033401